Chemical Engineering Journal 526 (2025) 171198

Contents lists available at ScienceDirect

Chemical Engineering Journal

journal homepage: www.elsevier.com/locate/cej

3-component (N, Fe, Co) atomically dispersed ORR catalysts prepared by laser-driven decomposition of organic precursors

Ekaterina Pakrieva [a,b,c,*], Javier Hernandez-Ferrer [d], Gema Martinez [a,c,e], Francisco Balas [a,b,c], Enrique García-Bordeje [d], Alejandro Anson-Casaos [d], Laura Simonelli [g], Fernando Bartolome [a,h], Ana M. Benito [d], Wolfgang K. Maser [d], Jose L. Hueso [a,b,c,f,i,*], Jesus Santamaria [a,b,c,f,*]

[a] Instituto de Nanociencia y Materiales de Aragon (INMA) CSIC-Universidad de Zaragoza, Campus Rio Ebro, Edificio I+D, C/ Poeta Mariano Esquillor, s/n, 50018, Zaragoza, Spain
[b] Department of Chemical and Environmental Engineering, University of Zaragoza, Campus Rio Ebro, C/María de Luna, 3, 50018, Zaragoza, Spain
[c] Networking Research Center on Bioengineering, Biomaterials and Nanomedicine (CIBER-BBN), 28029, Madrid, Spain
[d] Instituto de Carboquímica (ICB-CSIC), Miguel Luesma Castan 4, 50018, Zaragoza, Spain
[e] Centro Universitario de la Defensa (CUD), Ctra. de Huesca, 50090, Zaragoza, Spain
[f] Instituto de Investigación Sanitaria (IIS) de Aragón, Avenida San Juan Bosco, 13, 50009, Zaragoza, Spain
[g] CELLS–ALBA Synchrotron, E-08290 Cerdanyola del Vallès, Barcelona, Spain
[h] Departamento de Física de la Materia Condensada, Universidad de Zaragoza, Pedro Cerbuna, 12, 50009, Zaragoza, Spain
[i] Escuela Politécnica Superior, Universidad de Zaragoza, Crta. de Cuarte s/n, 22071, Huesca, Spain

ARTICLE INFO

Keywords:
Oxygen reduction reaction (ORR)
Atomically dispersed metals
N-doped carbon
Laser pyrolysis
Activation treatment

ABSTRACT

The sluggish kinetics of the oxygen reduction reaction (ORR) remain a key bottleneck for the commercialization of proton exchange membrane fuel cells (PEMFCs), driving the search for efficient, non-precious metal catalysts. Herein, we present a laser-assisted pyrolysis strategy for the synthesis of nitrogen-doped carbon (NC) materials, both metal-free and containing atomically dispersed Fe and Co, using aerosolized phthalocyanine precursors and a near-instantaneous rapid decomposition under a high-energy laser beam, while preventing metal aggregation. A single-step post-synthetic thermal activation under an NH_3/N_2 atmosphere further tailors the textural and surface properties, without requiring ammonia co-feeding during laser pyrolysis, acid etching, or multiple treatments, marking a significant improvement over our previously reported single atom (Fe-N/C) protocols. The resulting Fe_Co/NC_tr catalyst exhibits high specific surface area, enhanced microporosity, improved graphitization, and increased abundance of electrochemically beneficial nitrogen sites. Compared to our earlier reported Fe–N/C catalysts, Fe_Co/NC_tr delivers significantly higher limiting current densities and enhanced durability in alkaline media. Overall, the developed Fe_Co/NC catalyst exhibits good ORR catalytic activity and outstanding long-term stability in alkaline media, comparable to the state-of-the-art commercial Pt/C catalysts. Cyanide poisoning tests confirm the essential role of atomically dispersed Fe^{2+} and Co^{2+} as active ORR sites.

1. Introduction

Polymer electrolyte membrane fuel cells (**PEMFCs**) are among the most promising technologies in the transition toward clean and sustainable energy, owing to their high efficiency and low emissions [1,2]. When powered by green hydrogen from water splitting, PEMFCs provide a reliable pathway for decarbonized energy conversion. However, the sluggish kinetics of the oxygen reduction reaction (**ORR**) at the cathode remains a key obstacle to their widespread commercialization. While platinum-based catalysts offer excellent performance, their high cost (nearly 20 % of the total fuel cell cost), scarcity, and limited durability represent significant challenges in their technological implementation [3–6]. This has spurred extensive efforts to develop alternative, non-precious metal catalysts for ORR.

* Corresponding authors at: Instituto de Nanociencia y Materiales de Aragon (INMA) CSIC-Universidad de Zaragoza, Campus Rio Ebro, Edificio I+D, C/ Poeta Mariano Esquillor, s/n, 50018, Zaragoza, Spain.
E-mail addresses: epakrieva@unizar.es (E. Pakrieva), jlhueso@unizar.es (J.L. Hueso), jesus.santamaria@unizar.es (J. Santamaria).

https://doi.org/10.1016/j.cej.2025.171198
Received 26 June 2025; Received in revised form 19 November 2025; Accepted 23 November 2025
Available online 24 November 2025

Among these alternatives, carbon-based materials have attracted great attention due to their excellent conductivity, chemical stability, and structural tunability [7–10]. However, they present a low interaction toward O_2 and ORR intermediates. Therefore, they typically undergo chemical tuning by introducing dopants or functional groups able to modify their surface properties. In this regard, doping carbon with light elements such as **N**, S or P that have similar atomic radius as carbon, induces charge density redistribution on the surface of carbon materials, which can effectively weaken the O—O bonding, leading to improved ORR performances [8,11,12]. Moreover, it has been shown that incorporating transition metals such as **Fe, Co,** or Ni can significantly enhance ORR activity by creating M–N_x coordination sites, where the metal acts as a highly active catalytic center [13,14].

Despite these advantages, transition metal-based catalysts often suffer from performance degradation due to metal leaching and limited conductivity [15]. To improve efficiency and long-term stability, single-atom catalysts (SACs) have been developed, offering high atomic utilization, well-defined active sites, and enhanced metal-support interactions [16–21]. However, obtaining single-atom (SACs) and dual-metal atom catalysts (DACs), where two different metal atoms synergistically contribute to catalysis, remains synthetically challenging due to the tendency of metals to aggregate into clusters or nanoparticles (NPs) [18–20,22].

In our previous work, we developed atomically dispersed Fe–N–C SACs [23], exhibiting good ORR activity, although stability issues were observed under accelerated stress testing. To improve on these results, in this work we adopted a dual-metal approach by introducing cobalt alongside iron. This is a logical strategy since cobalt is frequently paired with iron due to its complementary catalytic properties and electronic interactions. For instance, Li et al. [24] attributed the high activity of Fe—Co DACs to a reduced energy barrier for O—O bond dissociation, while Han et al. [25] demonstrated that the presence of both metals alters the charge distribution around the active sites, leading to an optimized electronic structure and enhanced catalytic performance. Dun et al. [26] associated the excellent ORR activity of their catalyst to the synergistic effect of dual metal sites, high specific surface area, and porous structure.

In addition to introducing a second metal, other strategies such as post-activation thermal treatments have often been used to enhance the performance of carbon-based catalysts [27–30]. Accordingly, in this work a single post-synthetic thermal treatment in an NH_3/N_2 atmosphere was applied following laser-assisted pyrolysis. This step enhanced the catalyst's surface area and porosity, crucial for mass transport and access to active sites, by partially gasifying the carbon matrix, removing volatile species. More importantly, the treatment also helped to stabilize the dispersed Fe and Co atoms, preventing aggregation and preserving their single-atom nature. Overall, this one-step activation played a crucial role in optimizing the catalyst's structure and boosting its long-term ORR performance in alkaline media.

As shown below, in this work a Fe_Co/NC catalyst was prepared, featuring atomically dispersed Fe and Co species within a nitrogen-doped carbon matrix, with a total metal loading of (0.45 ± 0.02 wt%). The post-synthetic treatment of the catalyst featuring atomically dispersed Fe and Co not only preserved metal dispersion in the carbon matrix, but also resulted in a solid displaying significantly improved physicochemical characteristic, namely higher specific surface area and increased microporosity in the sub-nanometer range.

Finally, while the materials were synthesized via laser-assisted pyrolysis, using the same aerosol-based feeding setup as in our previous study [23], in this case we performed important process modifications to facilitate processing and potential scale up. First, different phthalocyanine precursors were used for Fe and Co rather than combining them in a single molecule as a preformed bimetallic complex. This was intended to introduce flexibility regarding their relative concentrations, although the final metal ratios were influenced by their different solubilities in pyridine, as well as their distinct volatilities and decomposition behaviours under laser irradiation. These factors collectively governed the metal loading and dispersion in the resulting carbon matrix. Second, in contrast to our previously reported procedure for the synthesis of the Fe/NC material [23], the current process does not involve ammonia injection along with the phthalocyanine precursors, nor does it require subsequent acid etching or secondary thermal treatment, simplifying the process, making it more cost-effective and reducing operating costs. The main process-related advantages with respect to our previous work are schematically explained in Table S1.

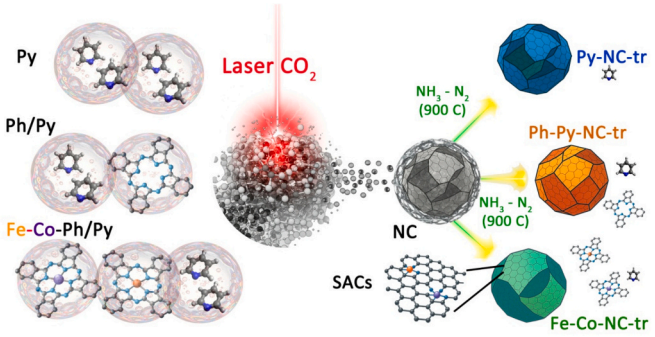

Scheme 1. Schematic representation of the different precursors used: metal-free systems based on pyridine (**Py**) as solvent, or phthalocyanine (**Ph**) in pyridine (**Ph/Py**); and dual-metal systems based on **Fe(Co)** phthalocyanine dissolved in pyridine and aerosolized for laser pyrolysis. The scheme also illustrates the applied post-synthetic treatments and the resulting sample nomenclature (**tr**), according to the precursor type.

In summary, the results of this work demonstrate the potential of laser pyrolysis to produce highly efficient, atomically dispersed catalysts containing different active species. In particular, the Fe_Co/NC catalyst delivered a substantially higher limiting current density, and clearly superior operational stability compared to the Fe/NC SACs catalyst, while maintaining a similar half-wave potential in alkaline media. These advancements are especially relevant for practical applications in membrane electrode assemblies for fuel cells, where high mass activity, efficient mass transport, and long-term durability are critical performance parameters. Of note, metal-free N-doped carbons were also synthesized as controls, and they demonstrated notable intrinsic ORR activity, highlighting the catalytic contribution of the nitrogen-doped carbon matrix. Nevertheless, the superior performance of the Fe—Co system confirms the additive and beneficial role of atomically dispersed Fe and Co active sites.

2. Experimental section

2.1. Laser-driven generation of carbon materials and activation treatment

The synthesis of the different carbon materials was carried out by laser-assisted pyrolysis of different aerosolized organic precursors (Scheme 1) in a continuous flow reactor, as described elsewhere [23,31–33]. Metal-free carbon materials were prepared using either pyridine (labeled as **Py/NC**) or 90 mg of solid phthalocyanine (hereafter **Ph_Py/NC**) dissolved in 25 mL of pyridine. To generate carbons containing Fe and Co, two separate solutions were prepared, containing 45 mg of the corresponding metal (II) phthalocyanine in 12.5 mL of pyridine, which were then mixed to obtain a total volume of 25 mL. The final solution was fed from a sealed chamber equipped with a nebulizer board (APC International, Ltd., Mackeyville, USA) operating at 1.65 MHz and 40 V, converting it into aerosol droplets (samples named after **Fe_Co/NC)**. Additional experimental details about the laser reactor configuration and reaction conditions can be found in the Supporting Information. The as-prepared materials were collected directly onto cellulose filters (F2044), with subsequent calcination treatment in a muffle furnace at 300 °C (1 °C min^{-1} heating ramp) for 3 h to remove incompletely

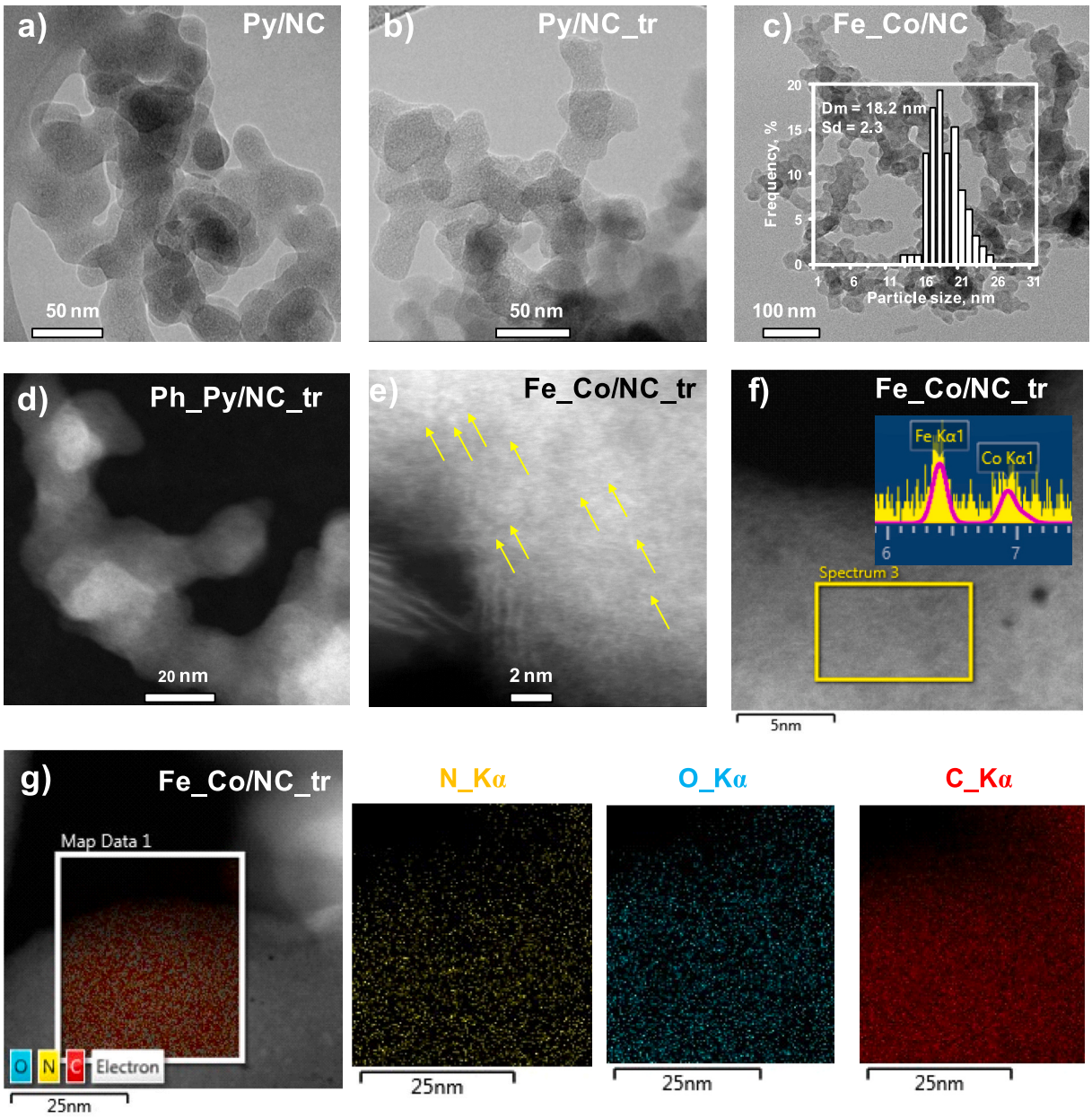

Fig. 1. Representative TEM images of Py/NC, Py/NC_tr and Fe_Co/NC materials (**a-c**), with inset showing particle size distribution (~18 nm) of the carbon nanoparticles; HAADF-STEM images of Ph_Py/NC_tr, Fe_Co/NC_tr (**d-f**) with inset in (**f**) showing EDX analysis, confirming the presence of Fe and Co in the Fe_Co/NC_tr material; Metal centers (Fe and Co) in HAADF-STEM (**e**) are highlighted with arrows. EDX elemental maps of the Fe_Co/NC_tr material (**g**) showing the spatial distribution of N, O, and C.

decomposed precursors.

The as-prepared samples (**Py/NC**, **Ph_Py/NC**, **Fe_Co/NC**) were subjected to a thermal activation treatment: first, under a N_2 flow (200 NmL min $^{-1}$) at 900 °C (heat ramp of 20 °C min^{-1}) and held at that temperature for 100 min, then, using a mixture of a NH_3/N_2 flow (30/200 NmL min^{-1}) at 900 °C for 30 min, followed by cooling down to the room temperature under a N_2 flow (200 NmL min $^{-1}$). The resulting catalysts were labeled as: **Py/NC_tr**, **Ph_Py/NC_tr**, and **Fe_Co/NC_tr.** In addition and for the sake of comparison, the Fe_Co/NC sample was treated for the last 30 min under N_2 atmosphere (200 NmL min $^{-1}$) in the absence of ammonia, under analogous experimental conditions. The resulting material was denoted as **Fe_Co/NC_inert tr**. The synthesis of these materials was performed by the Synthesis of Nanoparticles Unit (UNIT 9) of the ICTS "NANBIOSIS" at the Institute of Nanoscience and Materials of Aragon (INMA)-Universidad de Zaragoza. Additional experimental details (chemicals used, detailed laser pyrolysis set up, characterization methods (including X-Ray Absorption Spectroscopy carried out at the ALBA synchrotron) and electrochemical measurements are given in the Supporting Information.

3. Results and discussion

Drawing upon our established expertise in laser-driven catalyst synthesis, we developed a simplified and more cost-effective approach for the preparation of dual-metal (Fe, Co) atomically dispersed catalysts, labeled Fe_Co/NC. This method utilizes the near-instantaneous laser-driven decomposition of aerosolized suspensions of separate iron and cobalt phthalocyanine precursors in pyridine. This strategy, using commercially available precursors, offers flexibility in tuning metal ratios, limited only by their solubility. A key modification from our

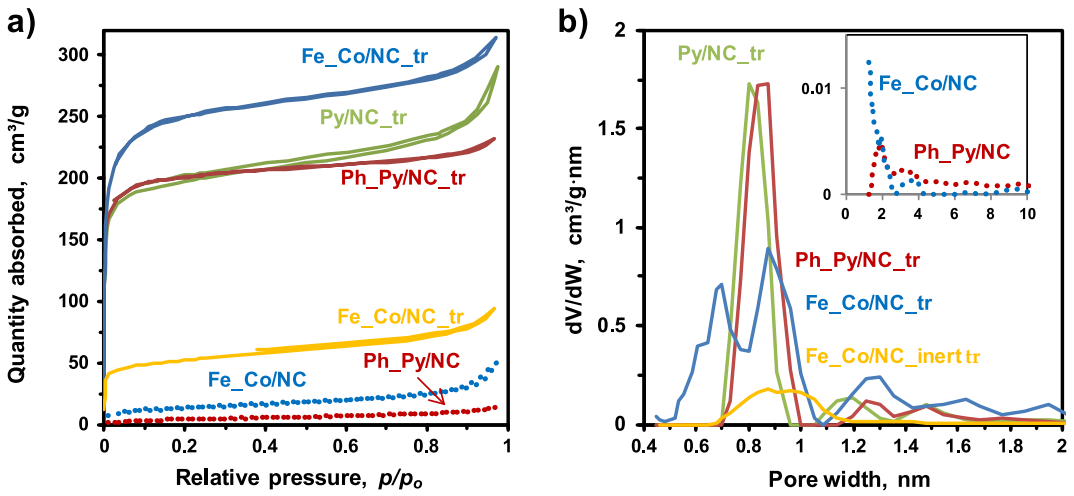

Fig. 2. N_2 adsorption (77 K) isotherms (**a**) and NLDFT pore size distributions (**b**) for non-treated and treated samples.

previous single-Fe catalyst synthesis is the elimination of ammonia co-feeding during laser pyrolysis and the subsequent acid etching and secondary thermal treatment steps. Instead, the as-prepared materials underwent a single, high-temperature (900 °C) post-synthetic thermal treatment under an NH_3/N_2 atmosphere. A control sample, Fe_Co/NC_inert tr, was treated under an inert N_2 atmosphere for comparison. This streamlined process reduces operational complexity and chemical usage while lowering overall preparation costs.

3.1. *Synthesis and characterization of metal-free and dual-metal Fe—Co on N-doped carbons*

Electron microscopy (Fig. 1) confirmed that all carbon materials exhibited a disordered structure, characterized by aggregates of small interconnected carbon particles, approximately 18 nm in size (Fig. 1a,c) that remained structurally unchanged after NH_3 activation (Fig. 1b,d). HAADF-STEM and EDX analysis of the treated Fe_Co/NC materials showed no evidence of nanoparticle or cluster formation (Fig. 1e), instead revealing isolated bright dots indicative of atomically dispersed Fe and Co (Fig. 1f). EDX mapping further demonstrated the uniform distribution of C, N and O throughout the structure (Fig. 1g). The Fe and Co signals appear at background levels, consistent with their atomic dispersion below the spatial resolution of EDX (Fig. S1).

ICP-OES analysis of the as-synthesized material before activation showed an Fe content of 0.48 wt%. The treated in NH_3/N_2 at 900 °C Fe_Co/NC material showed an Fe content of approximately 0.45 ± 0.02 wt%. Cobalt consistently exhibited lower incorporation than iron, being below the quantification limit, reflecting its limited solubility in the synthesis solvents and distinct decomposition behavior under laser irradiation. Under identical conditions, (91 mg of phthalocyanine in 25 mL of pyridine), only 11 mg of CoPh (~13 mol%) dissolved versus 25 mg of FePh (~29 mol%), resulting in 80 mg, and 66 mg of precipitate, respectively. The limited solubility of CoPh in pyridine, along with its different decomposition temperature, likely governed the final Fe:Co ratio in the atomically dispersed carbon network.

XRD patterns (Fig. S2a-b) revealed two characteristic broad diffraction peaks at ~25° and ~ 44° (2θ) for all catalysts, ascribed to the (002) and (100) planes of disordered carbon, respectively [34]. No signals attributable to crystalline Fe or Co phases were detected, (Fig. S2a-S2b), confirming the absence of metal clustering. Raman spectroscopy (Fig. S3a-S3b) showed that the intensity ratios of the disorder-induced D band at ~1350 cm^{-1} to the tangential stretch G band at ~1590 cm^{-1} (I(D)/I(G) [35] were similar for all metal-free samples, regardless of activation under N_2 or NH_3/N_2. However, the I(D)/I(G) ratio for the non-treated Fe_Co/NC sample was notably lower compared to all other materials and increased after activation treatments, aligning with values observed for all materials, and suggesting increased structural disorder after activation. DRIFTS results showed that non-treated samples hold a structure close to the activated carbon structure with the presence of nitrogen- and oxygen- functional groups (Fig. S4a), which were completely removed after NH_3 activation treatment (Fig. S4b), indicating significant chemical restructuring during thermal treatment.

The single post-synthetic thermal treatment, particularly under NH_3/N_2 atmosphere, significantly enhanced the textural properties of the materials. As shown in Fig. 2a, non-treated samples (dotted lines) exhibited type II isotherms, characteristic of non-porous or poorly porous materials [36], with BET surface areas below 50 m^2/g and low pore volumes (Table S2). After NH_3 activation at 900 °C, the metal-free materials (Py/NC_tr and Ph_Py/NC_tr) achieved BET surface areas exceeding 700 m^2/g. Notably, the incorporation of Fe and Co followed by NH_3/N_2 activation further increased the surface area of Fe_Co/NC_tr to 900 m^2/g, corresponding to a ~ 20-fold increase compared to its untreated form. In contrast, Fe_Co/NC treated under N_2 showed only a modest five-fold increase in surface area, highlighting the critical role of NH_3 in promoting microporosity and textural development. Additionally, non-local density functional theory (NLDFT) pore size analysis indicated a well-developed microporosity, with pore widths about 0.8 nm for Py/NC_tr and Ph_Py/NC_tr, and additional sub-nanometer pores (~ 0.7 and 0.9 nm) emerging in Fe_Co/NC_tr [37] (Fig. 2b). SEM images (Fig. S5) display agglomerated carbon particles with similar overall morphology before and after NH_3/N_2 activation, indicating that the large increase in BET surface area originates from micro- and mesoporosity not resolved at SEM magnifications.

The formation of microporosity after activation is a consequence of the thermal removal of carbon fractions, a process amplified by NH_3. As previously reported [38], ammonia interacts with disordered carbon phases during heat treatment, enhancing mass loss and ORR catalytic activity, although the mechanism was not specified. We suggest that in the presence of catalytic metal centers at high temperatures, as also demonstrated by Bota and Abotsi [39], ammonia undergoes in-situ decomposition to generate hydrogen (Reaction 1), which subsequently reacts with carbon (Reaction 2).

$$2NH_3 \rightarrow N_2 + 3H_2 \quad \text{(R1)}$$

$$C + 2H_2 \rightarrow CH_4 \quad \text{(R2)}$$

In addition to the above gas-evolving reactions, another mechanism likely contributing to the observed porosity increase is the elimination of volatile fractions that block the pores, originating from non-evaporated solvent residues or partially decomposed precursors. This would happen

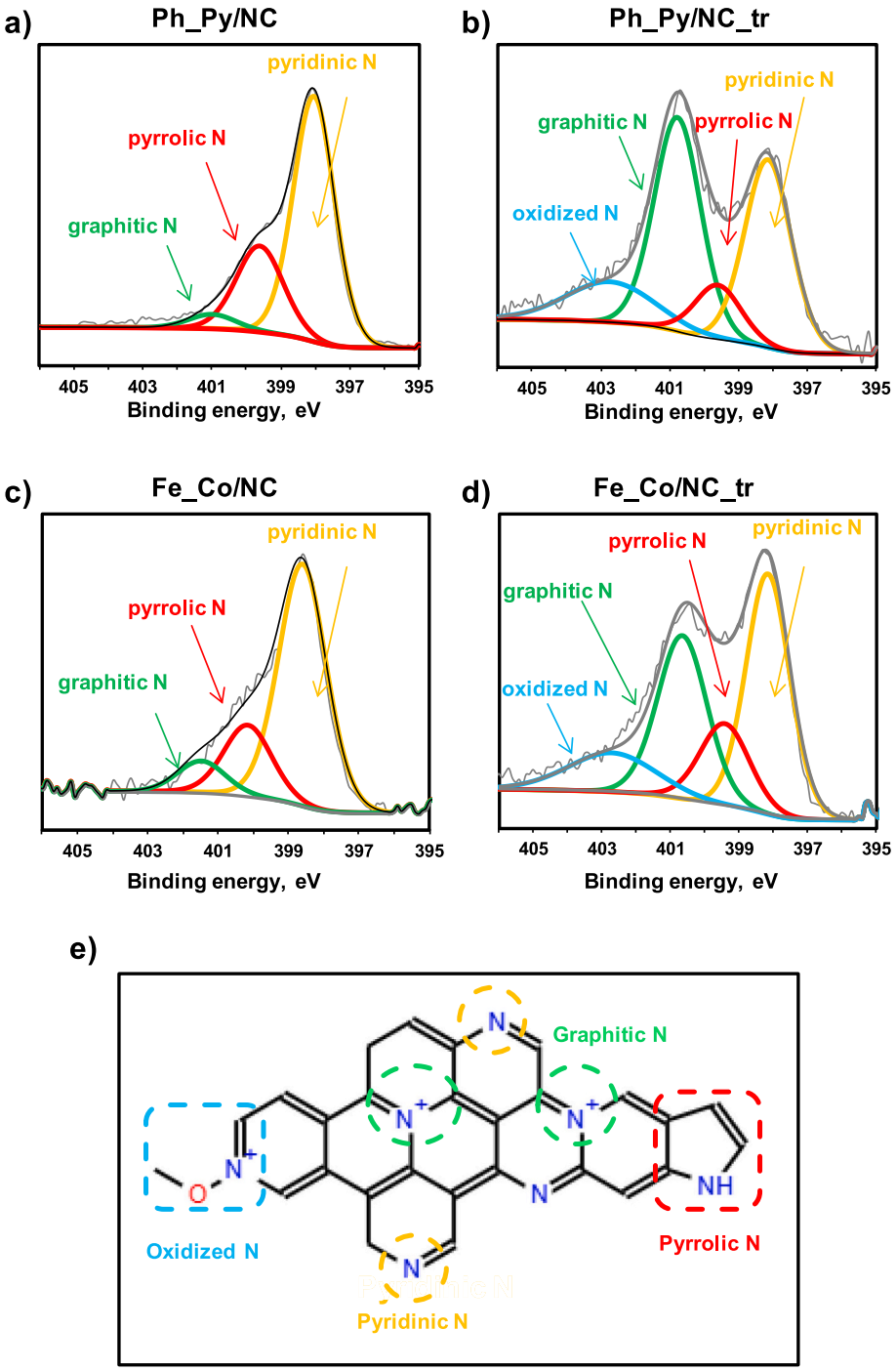

Fig. 3. X-ray photoemission spectra and fitting analysis corresponding to the N 1 s region for non-treated (**a,c**) and treated (**b,d**) samples and schematic representation of different types of nitrogen binding in carbon matrix **(e)**.

even under inert atmosphere and their removal during thermal activation would contribute to pore opening and the observed increase in surface area. TGA results (Fig. S6) support this interpretation: while both metal phthalocyanines exhibit ~90 % total mass loss by 640 °C, FePh begins to decompose at a much lower temperature (~380 °C), whereas CoPh starts decomposing closer to 550 °C. Moreover, as already mentioned, the solubility of CoPh in pyridine is significantly lower (13 mol%) compared to FePh (29 mol%), which, together with the higher decomposition temperature, may result in incomplete incorporation of Co species, leaving residual organics that are removed during activation. Thus, porosity development results from both metal-catalyzed gasification of carbon structure under NH_3 and thermal volatilization of organic residues.

These results are in agreement with XRD, DRIFTS and especially XPS analysis (vide infra), indicating progressive carbonization concurrent with a decrease in the surface concentration of N and O in the treated samples. Increased carbonization entails higher electrical conductivity, facilitating electron transfer [40]. Moreover, a higher porosity and larger specific surface area increase the contact surface, exposing more electrochemically active sites [41–43].

XPS analysis confirmed a significant presence of C, O, N species, with no signals detected in the Fe and Co regions (Table S3). This absence is attributed to the low amounts of metal present in the samples, which fall below the detection limit of the technique.

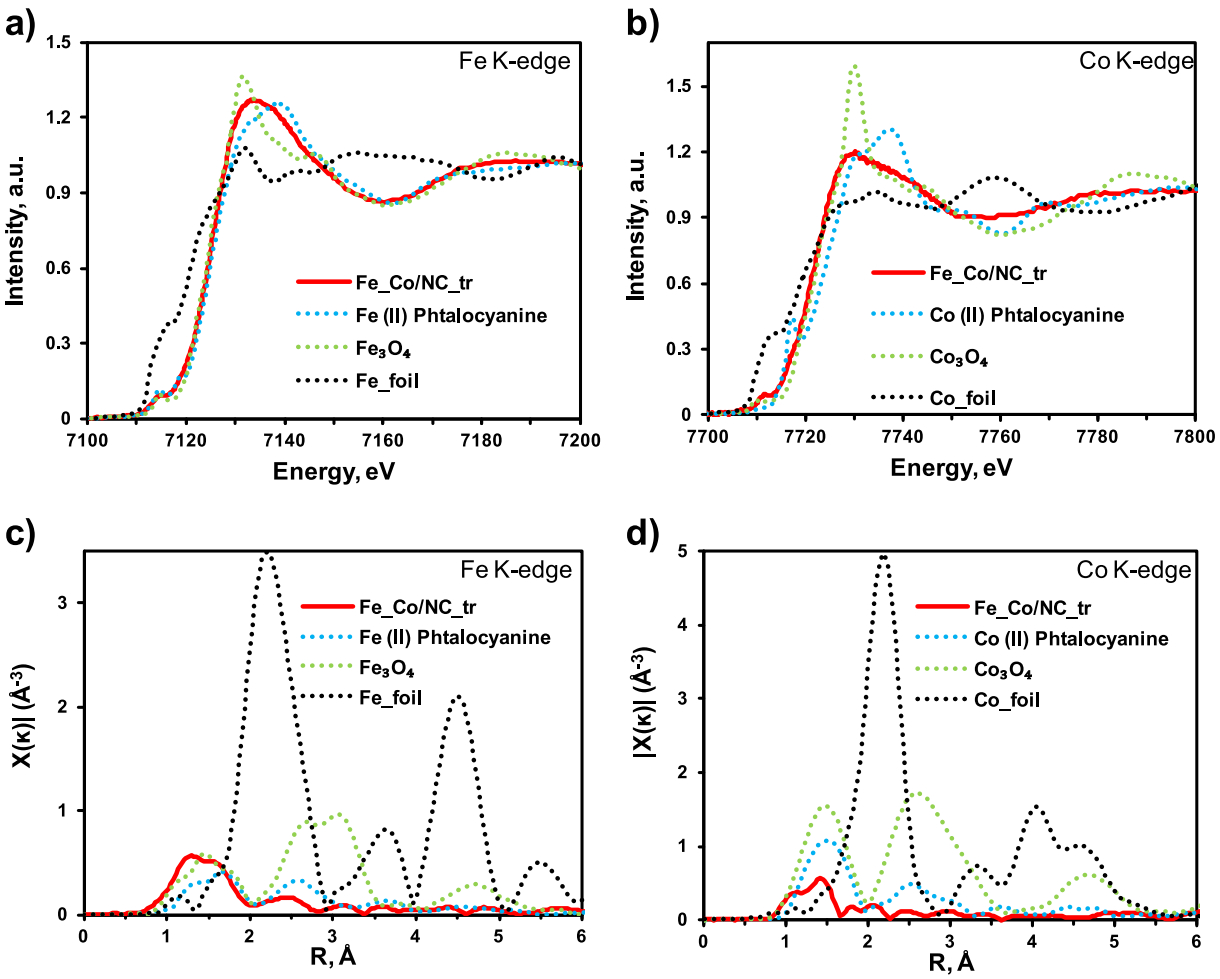

Fig. 4. Normalized Fe (**a**) and Co (**b**) K-edge XANES spectra collected on the Fe_Co/NC_tr system and compared with references (Fe(*II*)Phthalocyanine, Fe_3O_4, Fe metal, Co(*II*)Phthalocyanine, Co_3O_4, Co metal). (**c, d**) Fourier transforms of the corresponding k^2-weighted EXAFS spectra performed with a sine window between 2.65 and 14.5 $Å^{-1}$.

A slight decrease in N and O atomic concentrations was found for the samples after activation treatments. Additionally, trace amounts of S, and F impurities (0.05 at.%) were detected in Ph_Py/NC_tr in samples, originated from SF_6, which was used as a photosensitizer to selectively absorb infrared laser wavelengths during synthesis. Detailed analysis of the fitted X-ray photoemission spectra corresponding to the N 1 s region (Fig. 3 and Fig. S7)) indicated the coexistence of pyridinic-N, pyrrolic-N, quaternary-N in all samples, along with the progressive appearance of oxidized-N in the treated catalysts [44–46]. Furthermore, pyridinic-N and pyrrolic-N were converted into thermodynamically more stable graphitic-N (quaternary-N) after treatment (Table S4).

In the C 1 s region spectra (Fig. S8), the most pronounced peak around 284.5 eV, is assigned to C—C bonds, primarily containing sp^2 carbon [47]. C—N and C—O bonding were ascribed at 286 eV, while minor signals attributed to carboxylic groups (O=C-OH, 287.9 ± 0.3 eV) and to π–π* interactions (290.4 ± 0.2 eV) were also fitted [45,46,48]. The relative percentage of the different carbon species for C 1 s is summarized in Table S5. It can be seen that following the activation treatment, C-O/C-N and O=C-OH decrease in correspondence with the removal of nitrogen and oxygen atoms from the carbon matrix. In contrast, the contribution of sp^2 C and π-π* graphitic shake-up satellite increased, being more noticeable for the Fe_Co/NC_tr sample, indicating an enhanced graphitization degree [49], which we attribute to the NH_3 activation treatment, especially in the presence of metals.

Fig. 4 reports the Co and Fe K-edge X-ray absorption spectra collected over the treated Fe_Co/NC material and compared with different Fe and Co references. Fig. 4a-b depicts the normalized x-ray absorption near edge structure (XANES), while Fig. 4c-d correspond to the Fourier transform (FT) of the k^2-weighted extend x-ray absorption fine structure for the Fe and Co K-edge, respectively. The Fe and Co K-edge XANES features corresponding to the Fe_Co/NC samples landed in between the Fe and Co phthalocyanine and oxides spectra, suggesting a global Fe and Co oxidation state close to 2+. The main signal contribution to the FTs for both the Fe and Co K-edge appears in between 1 and 2 Å, in correspondence of the first shell of the corresponding phthalocyanine and oxide references. This first shell contribution, around 1.4 Å, is attributed to the M-O/C/N bond (M = Fe or Co). In the reference spectra, the second contribution appearing around 2.5 Å corresponds to the second shell, to the M-M bond. Its strong suppression for the sample spectra indicates that Fe and Co are atomically dispersed. At both the Fe and Co K-edges, the first shell is structured, suggesting the M coordination with light elements (O/C/N) at slightly different distances. At the Co K-edge the global intensity of the first shell contribution is strongly reduced respect to the references, indicating a global higher local disorder.

3.2. *Electrochemical measurements*

The prepared carbon materials were tested in the electrocatalytic oxygen reduction reaction (ORR) using a rotating disk electrode (RDE). Key ORR parameters, such as onset potential (E_{onset}, V), limiting current density (j_L, mA ·cm^{-2}), and half-wave potential ($E_{1/2}$, V), were determined from the recorded linear sweep voltammetry (LSV) polarization

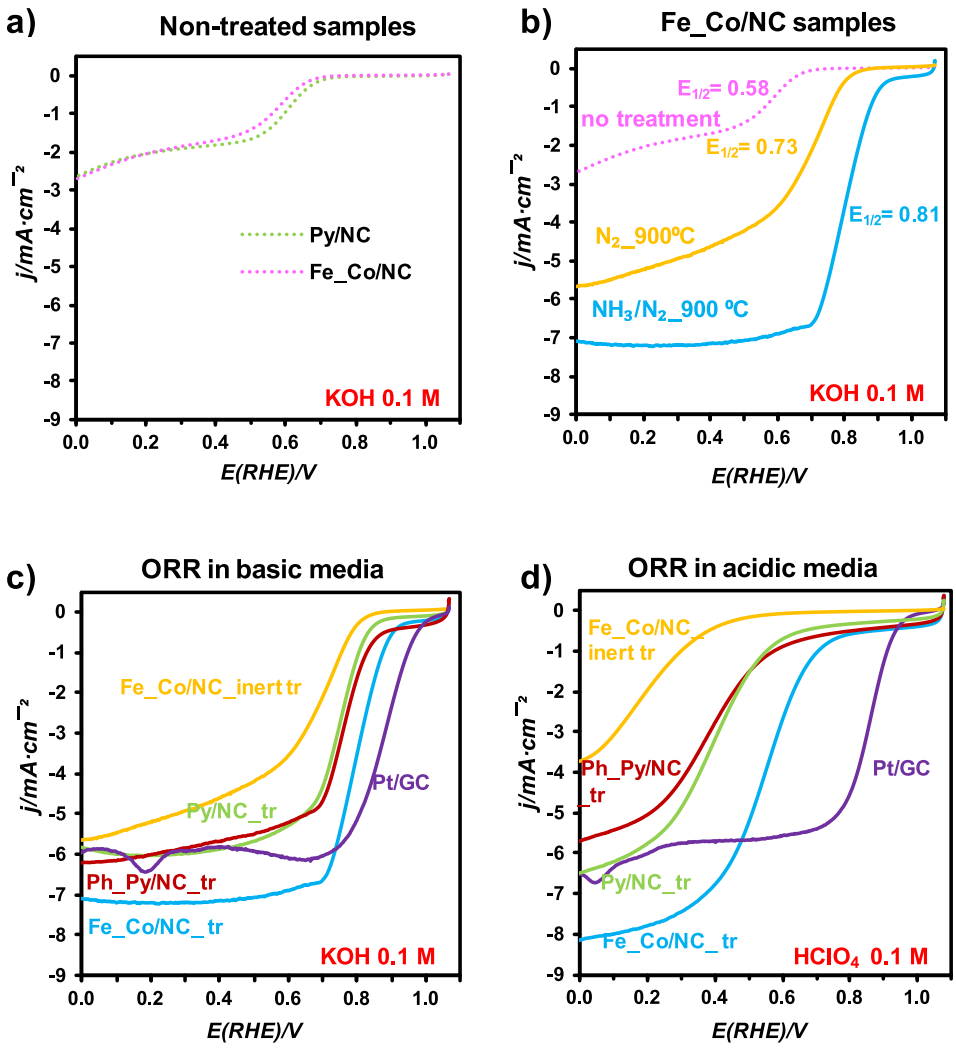

Fig. 5. ORR polarization curves for non-treated samples (**a**), for the *Fe_Co/NC samples* under different conditions (**b**), treated samples vs. commercial Pt/GC catalyst in alkaline (**c**) and acidic (**d**) electrolyte. All linear sweep voltammetry (LSV) tests were collected at a sweeping rate of 10 mV s^{-1} and at a rotating speed of 1600 rpm.

curves. The onset potential, defined as the potential where the electrochemical process begins, was determined through baseline correction of capacitive currents and applying a current threshold of −0.1 mA·cm^{-2} [50]. The limiting current density is the maximum current achievable by a cell as the concentration of reactant O_2 at the electrode working surface approaches zero, providing an estimation of oxygen mass transport resistance [51], i.e. the mass diffusion-controlled region. The half-wave potential reflects the coupling behavior of surface reaction kinetics and mass diffusion; serving as a metric to evaluate the activity of the electrocatalyst [52]. The apparent number of electrons transferred per O_2 molecule was calculated using the first-order Koutecky–Levich equation, as described in the Supporting Information.

3.2.1. *Reaction in basic media*

Electrocatalysts based on carbon typically demonstrate optimum performance in alkaline media [53–55] and therefore, our electrocatalysts were tested in an alkaline solution (0.1 M KOH, pH ~ 13) and compared with other catalysts under equivalent conditions. Non-treated samples, regardless of composition, showed inferior ORR activity characterized by low limited current density, low $E_{onset}/E_{1/2}$, and the predominance of hydrogen peroxide generation via the two-electron pathway (Reaction 3, Fig. 5a, Table S6, entries 1–2).

$$O_2 + \mathbf{2\,e^-} + H_2O \rightarrow HO_2^- + OH^- \quad \text{(R3)}$$

$$O_2 + \mathbf{4\,e^-} + 2\,H_2O \rightarrow 4OH^- \quad \text{(R4)}$$

In contrast, activation treatments, particularly those involving NH_3, resulted in significant enhanced ORR activity (Fig. 5b,c and Table S6). These metal-free N-doped carbon materials showed performance comparable to a commercial Pt/GC catalyst used for comparison, achieving limiting current density values of 6 mA*cm^{-2} and a clear preference for the four-electron pathway (Reaction 4, Fig. 5c, Table S5, entries 4–5). Notably, the Fe_Co/NC_tr catalyst outperformed the Pt/GC catalyst in terms of limiting current density (7.08 vs 5.98 mA*cm^{-2}) although with slightly lower E_{onset} (0.92 vs 0.99 V), and a less positive half-wave potential (0.81 vs 0.88 V) (Table S6, entries 6–7).

To elucidate the role of ammonia, a control activation treatment under pure N_2 at identical conditions was applied. These samples showed moderate improvement over non-treated ones, but their ORR activity remained significantly lower than those activated in the presence of ammonia (Fig. 5b), highlighting the crucial role of ammonia in enhancing catalyst performance.

3.2.2. *Reaction in acidic media*

Additionally, the ORR performance of the treated samples was tested in an acidic electrolyte (0.1 M $HClO_4$, pH ~ 1), which typically exhibits slower ORR kinetics compared to the alkaline environment [56,57]. Nevertheless, acidic PEMFCs are increasingly favored for large-scale applications due to their higher power density and superior long-term

stability compared to alkaline PEMFCs [58]. In acidic conditions, a similar activity trend was observed among the studied electrocatalysts (Fig. 5d, Table S7): Fe_Co/NC_tr > Ph_Py/NC_tr ≈ Py/NC_tr Fe_Co/NC_inert tr. Here, the determination of the water formation (Reaction 5, vide infra) was based on the calculated number of transferred electrons. Notably, the Fe_Co/NC_tr catalyst exhibited a higher limiting current density (8.15 vs. 6.52 mA·cm^{-2} for commercial Pt/GC). However, its significantly lower onset potential (0.76 vs. 0.96 V) and half-wave potential (0.59 V vs. 0.87 V) in acidic media (Table S7, entries 4 and 5) highlight its intrinsically lower ORR activity. This observation aligns with reports on the reduced stability and activity of non-precious metal catalysts in acidic media due to demetallation and slow proton-coupled electron transfer, apart from the carbon corrosion or oxidation as the main cause of the degradation [59]. In contrast, Pt-based catalysts remain active and stable across both environments due to their optimal ORR intermediate binding energies and strong corrosion resistance [60]. At the same time, recent work has demonstrated that optimizing the local coordination and symmetry of FeN_4 sites by introducing asymmetric edge-carbons can significantly enhance their ORR performance in acidic environments by modulating the electronic structure of the Fe centers [61].

$$O_2 + 4\,e^- + 4H^+ \rightarrow 2\,H_2O \quad \text{(R5)}$$

Comparing these results with our previous work on single-atom Fe-C/N catalysts [23], where Fe–N@C–NH_3 materials were synthesized using iron phthalocyanine with ammonia injected during the laser-assisted pyrolysis step, followed by a multi-step activation process including acid etching and subsequent post-activation thermal treatments (one or two), the current study presents a significantly improved approach. Here, we developed a dual Fe—Co atomically dispersed ORR catalyst (Fe_Co/NC) by employing separate Fe and Co phthalocyanine precursors for flexibility, eliminating ammonia co-feeding during the initial laser pyrolysis step, and crucially, simplifying the post-synthetic activation to a single thermal treatment under NH_3/N_2 atmosphere, thereby avoiding the previously required acid etching and second thermal treatment steps. Compared to the previous single-metal Fe-N@C-NH_3 1HT (one thermal treatment step) and 2HT (two thermal treatment steps) catalysts (with ~0.1 wt% Fe loading), the current dual-metal Fe_Co/NC_tr catalyst (with a total metal loading of 0.45 wt% ± 0.02) demonstrates notable enhancements. Although the previous catalysts showed comparable E_{onset} and $E_{1/2}$ potentials to Fe_Co/NC_tr (Table S6, entries 6, 8, 9; Table S7, entries 4, 6, 7), the Fe_Co/NC_tr catalyst delivered substantially higher limiting current densities in both alkaline and acidic conditions. This performance gain is particularly significant in acidic electrolyte, where Fe_Co/NC_tr achieved 8.15 mA·cm^{-2}, starkly contrasting with the lower values of 2.60 mA·cm^{-2} for Fe-N@C-NH_3 1HT and 3.60 mA·cm^{-2} for Fe-N@C-NH_3 2HT (Table S7). This represents a remarkable ~40–70 % increase in limiting current density, indicative of improved mass transport and greater accessibility of active sites in the Fe_Co/NC_tr material.

To monitor hydrogen peroxide formation during the ORR, rotating ring-disk electrode (RRDE) measurements were performed using a glassy carbon disk equipped with a Pt ring. The study includes the bimetallic Fe_Co/NC_tr catalyst as well as the control monometallic Fe/NC_tr and Co/NC_tr samples, all prepared, treated and tested under identical conditions together with metal-free Ph_Py/NC_tr and commercial Pt/GC. Among the studied catalysts, the metal-free Ph_Py/NC_tr exhibits the lowest ORR activity in both alkaline and acidic media (Fig. S9). The bimetallic Fe_Co/NC_tr shows the highest limiting current density, while its half-wave potential and electron transfer number (3.9 or ~ 7 % of H_2O_2 at 0.65 V vs RHE) are comparable to those of the monometallic Fe/NC_tr and Co/NC_tr samples, except in acidic media, where Co/NC_tr generates more H_2O_2 (up to 28 % Fig. S9e), indicating the lowest selectivity among all catalysts.

The stability of the Fe_Co/NC_tr catalyst and its metal-free support after activation treatment was evaluated using load cycling accelerated

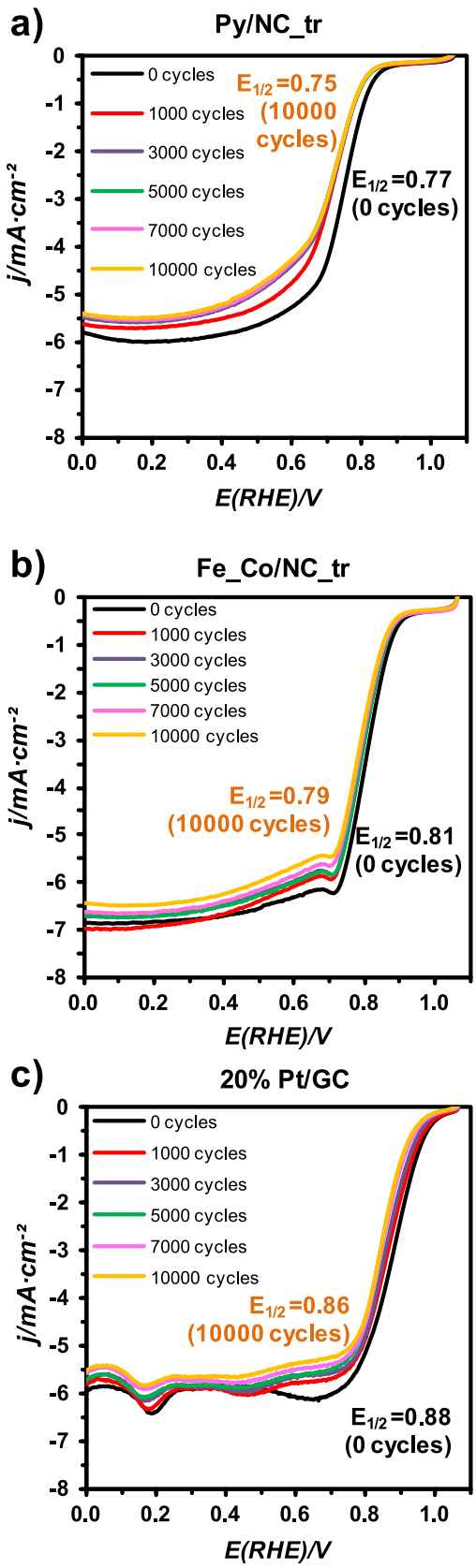

Fig. 6. ORR polarization curves of treated samples and 20 % Pt/GC before and after stability tests in KOH 0.1 M measured at 1600 rpm.

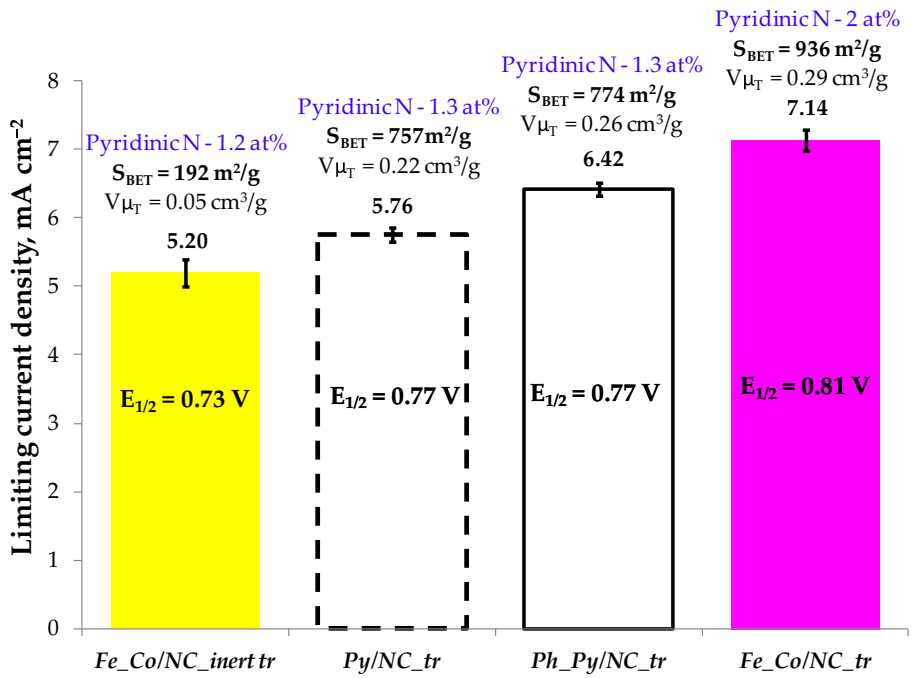

Fig. 7. Trends found in textural and surface properties and ORR results. VμT – total micropore volume.

stress tests (AST) and compared with the performance of commercial Pt/GC (Fig. 6). Remarkably, after 10,000 cycles, all samples, including Fe_Co/NC_tr, the support, and Pt/GC showed only a 7–8 % loss in limiting current density and a 20 mV decrease in half-wave potential. In contrast, under the same AST conditions, the previously reported Fe–N@C–NH_3 (2HT) catalyst exhibited a 15 % loss in limiting current and a comparable 20 mV drop in half-wave potential. These results demonstrate the superior durability of the Fe_Co/NC system and, combined with its enhanced catalytic activity and simplified, cost-effective synthesis, highlight its significant advantages over the previous Fe–N/C catalysts.

To further investigate ORR performance in acidic media, accelerated stability tests (ASTs) were performed using RRDE for metal-free Ph_Py/NC_tr, bimetallic Fe_Co/NC_tr, and commercial Pt/GC. The metal-free sample showed the largest loss in half-wave potential (~100 mV), Fe_Co/NC_tr experienced moderate degradation (~30 mV), and Pt/GC remained largely stable (Fig. S13). Post-cycling HAADF-STEM confirmed that Fe and Co remain atomically dispersed, indicating minimal metal leaching (Fig. S14). These results suggest that the lower activity and gradual degradation in acidic media mainly originate from the chemical instability of the N-doped carbon framework, involving partial oxidation or corrosion of the carbon support [59]. The presence of atomically dispersed Fe and Co species appears to mitigate these effects to some extent by stabilizing the carbon matrix and maintaining the integrity of active sites.

The activation treatment in the presence of NH_3 results in a variety of effects on the catalyst that draw a complex picture. On the one hand, the total N content decreases significantly after treatment, likely a consequence of the high temperatures employed, since a similar decrease is also observed for the treatment in the absence of NH_3. However, the treatment produces a profound change on the relative contribution of the different N species, with strong increases for the quaternary and oxidized nitrogen. On the other hand, perhaps the most significant change refers to the increase of the BET surface area and the development of microporosity.

Additionally, electrochemically active surface area (ECSA) of the treated catalysts immobilized on glassy carbon electrode was determined based on the double-layer capacitance recorded using CV in an Ar-saturated 0.1 M KOH solution, in a potential range where there is minimal faradaic current response. Therefore, the ECSA represents the area of the electrode material accessible to the electrolyte, while S_{BET} areas are obtained by measuring powders through gas adsorption. The ORR performance correlated well with both the BET surface area and ECSA (Fig. 7 and Table S8), supporting the importance of accessible surface area and porosity.

Based on the characterization results, it became evident that the NH_3 activation treatment at 900 °C led to partial gasification and carbonization of the (Fe_Co)/NC samples, resulting in the development of high surface area and porosity, along with the formation of active and stable sites. Previous studies suggest that a higher fraction of **pyridinic N species** can increase current density, spin density, and the density of π states near the Fermi level, thereby boosting O_2 reduction [62–64]. In this respect, our catalyst with the highest activity (Fe_Co/NC_tr) also exhibited the highest pyridinic N content among all the samples (around 2 at.%) (Fig. 7 and Table S3). However it should be noted that the pyridinic N content actually decreases after treatment, which suggests that other N species, particularly quaternary and oxidized nitrogen, that increase strongly after treatment (Table S4), also contribute to the observed electrochemical performance. Interestingly, the best performing catalyst Fe_Co/NC_tr, also displayed a strong π-π* graphitic shake-up satellite signal in the C 1s region, indicating a higher graphitization degree (Fig. S5 and Table S5), which facilitates transport. Together with enhanced porosity, these features improve O_2 diffusion and mass/electron transfer, improving ORR kinetics [42].

In summary, while it is difficult to disentangle the combined effects of the different features of the catalyst, some general trends can be identified. Specifically, higher specific surface area and porosity, along with larger nitrogen content, especially in terms of pyridinic nitrogen, correlates with higher ORR performance, particularly regarding limiting current density and half-wave potential (Fig. 7). These trends are further supported by control experiments with the corresponding monometallic samples, which confirm the role of balanced porous texture, including the microporous contribution, nitrogen functionalities, and atomic metal dispersion (Fig. S10-S12, Tabl S9-S10), rather than a pronounced Fe—Co synergistic effect. A similar relationship between nitrogen speciation, hierarchical porosity, and ORR performance was reported by Zhang et al. [65] for Co–Cu/NC catalysts, where enhanced N-doping efficiency and coexistence of micro- and mesopores promoted active-site

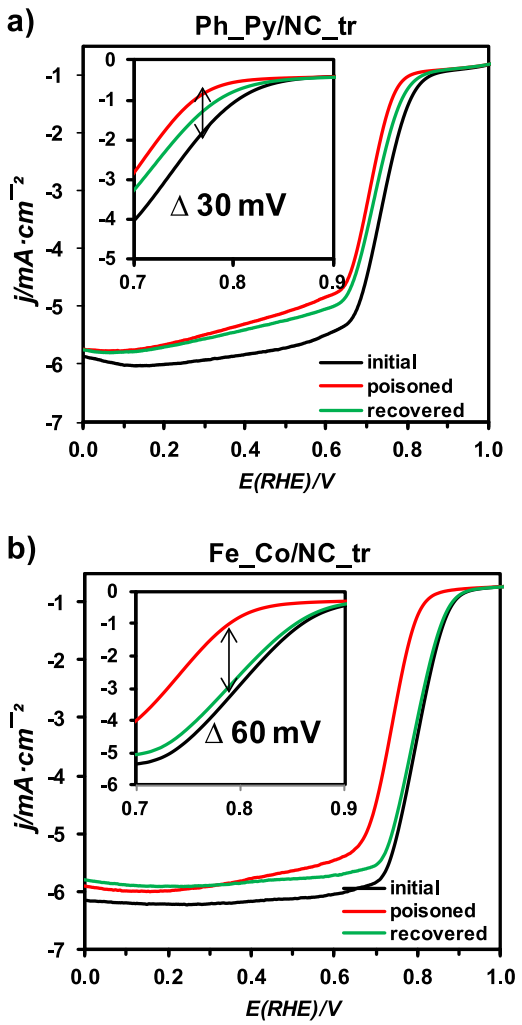

Fig. 8. ORR polarization curves for electrodes before (black line), after (red line) **poisoning** with 10 mM KCN, and after rinsing with water (green line) in O_2-saturated 0.1 M NaOH. Data recorded at 1600 rpm, 10 mV sec^{-1}.

accessibility and reaction kinetics.

Finally**, poisoning tests with KCN** were applied to further corroborate the role played by metal centers in the observed catalyst performance. Cyanide is known to form very strong complexes with metal ions, deactivating metal-based active sites and thus, hindering the ORR at the M^+ centers [66]. Notably, the Fe_Co/NC_tr catalyst exhibited a clear decrease of ORR activity after KCN exposure (Fig. 8, Table S11), with near-complete recovery after rinsing the electrode with water in fresh electrolyte without cyanide, surpassing the performance of the metal-free support (Table S11, entry 4). In contrast, the Fe_Co/NC_inert tr sample (Table S11, entry 1) showed minimal activity loss, behaving similarly to metal-free supports (Table S11, entries 2–3). This confirms that NH_3 activation promotes the formation of accessible, catalytically active Fe^{2+}/Co^{2+} centers, which are absent in the Fe_Co/NC_inert tr sample. Similar findings have been reported [67], where an Fe loading of only 0.08 wt% delivered excellent ORR performance and stability, showing negligible effects of SCN^- poisoning and acid treatment, suggesting that the accessibility and dispersion of active sites, together with the N-doped carbon matrix, are more decisive than the absolute metal content.

Fig. 9 compares our best-performing catalyst with state-of-the-art carbon-based ORR electrocatalysts, including metal-free [40,68–70], single-metal (Fe [23,40,68,73,74], and Co [40,68,75–77]), and dual-metal systems (Fe_Co) [40,68,71,72]. While onset and half-wave potentials of our top electrocatalysts are in line with leading reports (Fig. 9a,b), Fe_Co/NC_tr stands out with superior limiting current density (Fig. 9c), indicating superior mass activity and enhanced active site accessibility.

4. Conclusions

This work demonstrates a laser-driven pyrolysis approach for synthesizing atomically dispersed dual-metal (Fe, Co) catalysts embedded in nitrogen-doped carbon. The method employs commercially available metal phthalocyanines dissolved in pyridine to form an aerosol, offering a cost-effective and flexible route that avoids complex bimetallic precursor synthesis and allows tuning of the metal ratio within solubility limits. The same procedure with either pyridine or a solution of phthalocyanine in pyridine can be used to prepare metal-free nitrogen-doped carbon-based catalysts.

Building upon previous work single-metal systems, the synthesis was significantly improved by using separate Fe and Co precursors and, importantly, by simplifying the post-synthetic activation to a single thermal treatment under an NH_3/N_2 atmosphere, eliminating the need for ammonia co-feeding during pyrolysis, and the subsequent acid etching, and second thermal treatment steps required previously, resulting in a more cost-effective process. The controlled laser synthesis followed by this specific single thermal treatment at 900 °C resulted in a material (Fe_Co/NC_tr) containing atomically dispersed Fe and Co sites, a remarkably high specific surface area (> 900 m^2/g), and enhanced microporosity, far exceeding the textural properties of earlier single-metal materials. These textural improvements, along with favorable modifications in nitrogen species and increased graphitization, significantly improved mass transport and active site accessibility.

Electrochemical studies revealed that the Fe_Co/NC_tr catalyst exhibits robust electrocatalytic activity, particularly in terms of high limiting current density and exceptional durability in alkaline media. Importantly, the catalyst retains over 92 % of its activity after extended 10,000 cycling, underscoring its long-term operational stability at a level comparable to commercial Pt/C. The metal content plays a crucial role, as iron and cobalt act as catalysts for the activation process during the thermal treatment, facilitating the formation of active centers (Fe^{2+}, Co^{2+}) key for ORR, as evidenced by poisoning tests with potassium cyanide.

Overall, this study provides a practical framework for designing dual-atom catalysts with superior stability and performance. The insights gained offer valuable guidance for future development of non-precious metal catalysts tailored for scalable deployment in proton exchange membrane fuel cells and other energy conversion technologies.

CRediT authorship contribution statement

Ekaterina Pakrieva: Writing – review & editing, Writing – original draft, Validation, Investigation, Funding acquisition, Formal analysis, Data curation. **Javier Hernandez-Ferrer:** Writing – review & editing, Validation, Supervision, Methodology, Investigation, Formal analysis, Data curation. **Gema Martinez:** Supervision, Methodology, Formal analysis, Conceptualization. **Francisco Balas:** Writing – review & editing, Validation, Methodology, Investigation, Formal analysis. **Enrique García-Bordeje:** Writing – review & editing, Validation, Supervision, Resources, Project administration, Funding acquisition, Formal analysis. **Alejandro Anson-Casaos:** Writing – review & editing, Visualization, Validation, Methodology, Investigation, Formal analysis, Data curation. **Laura Simonelli:** Writing – review & editing, Methodology, Formal analysis, Data curation. **Fernando Bartolome:** Visualization, Validation, Investigation, Formal analysis. **Ana M. Benito:** Writing – review & editing, Validation, Supervision, Resources, Funding acquisition. **Wolfgang K. Maser:** Writing – review & editing, Validation, Supervision, Resources, Funding acquisition. **Jose L. Hueso:** Writing – review & editing, Visualization, Supervision, Resources, Project administration,

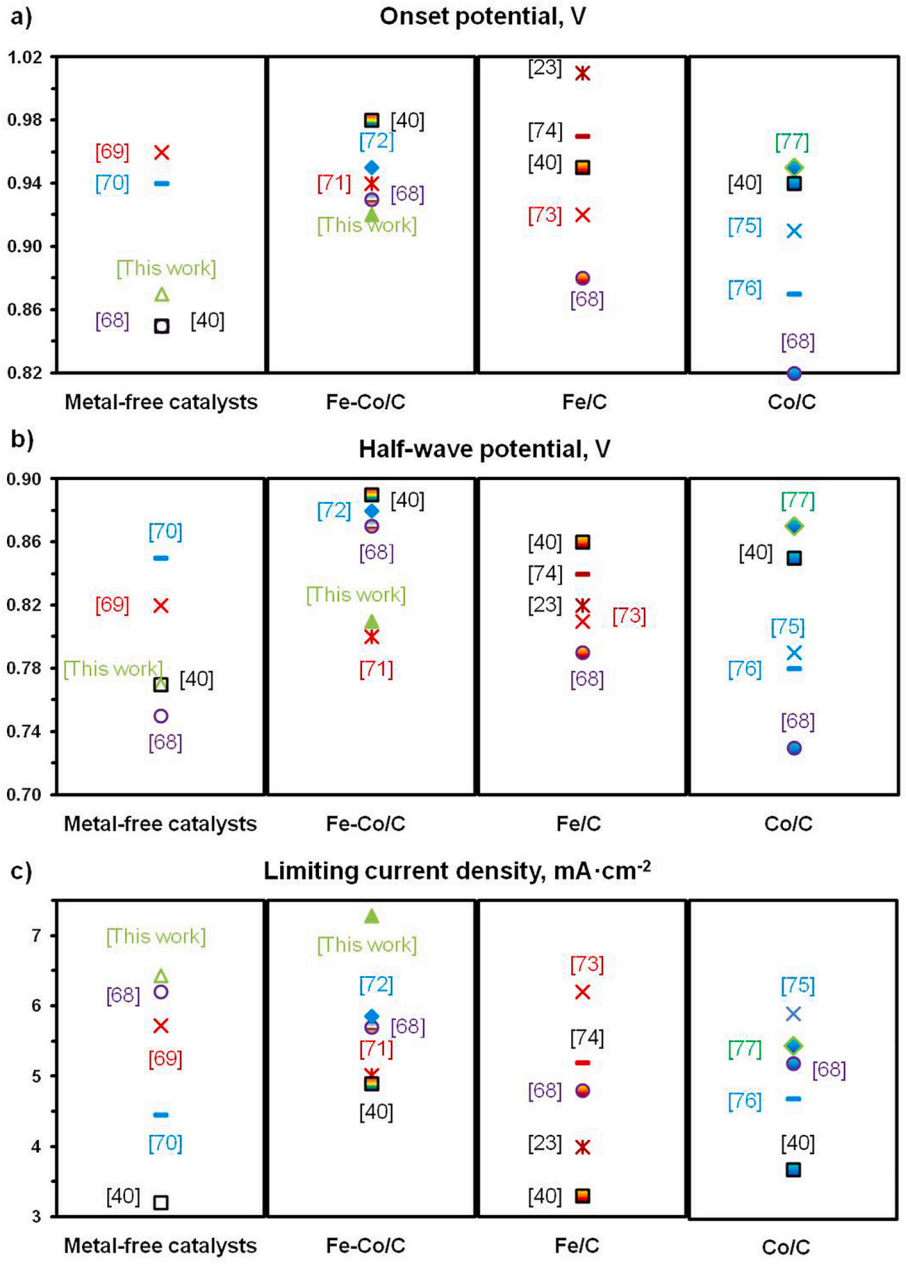

Fig. 9. ORR performance comparison of different electrocatalysts in 0.1 M KOH at 1600 rpm.

Methodology, Investigation, Funding acquisition, Conceptualization. **Jesus Santamaria:** Writing – review & editing, Validation, Supervision, Resources, Project administration, Investigation, Funding acquisition, Conceptualization.

Declaration of competing interest

The authors declare that they have no known competing financial interests or personal relationships that could have appeared to influence the work reported in this paper.

Acknowledgments

The authors thank funding from the Spanish Research Agency and MICN/AEI (projects CNS2022-135911 (J.L.), PID2020-114926RB-I00 (J.S.), PID2022-139671OB-I00 (W.M. and A.B) and PID2023-146481OB-I00 (E.G.). Severo Ochoa funds (CEX2023-001286-S) are acknowledged by MICIU/AEI/10.13039/501100011033. Financial support from Diputación General de Aragón under project T57_23R (J. S.) and T03_23R (W.M., A.B., E.G., A.A.) (Grupos Reconocidos), Project "ERDF A way of making Europe" by the European Union is gratefully acknowledged. EP thanks Juan de la Cierva Formación postdoctoral fellowship (JDC2022-049007-I) financed by MICIU/AEI/10.13039/501100011033 and by the European Union "NextGenerationEU"/PRTR".

The synthesis of materials has been performed by the Platform of Production of Biomaterials and Nanoparticles of the NANBIOSIS ICTS, more specifically by the Nanoparticle Synthesis Unit (Unit 9) of the CIBER in Bioengineering, Biomaterials & Nanomedicine (CIBER-BBN).

The authors acknowledge the use of instrumentation and technical support provided by the National Facility ELECMI ICTS, node 'Laboratorio de Microscopías Avanzadas (LMA)' at the Universidad de Zaragoza. Specifically, we thank Dr. Rodrigo Fernández-Pacheco for assistance with TEM studies, Dr. Fernando Cazaña and Dr. Guillermo

Antorrena for XPS data acquisition, Dr. Gala Simon for SEM measurements and Nuria Navascués for performing XRD, BET, and Raman analyses. The XAS experiments were performed at the CLAESS beamline of the ALBA synchrotron (proposal number 2022097042) with the support of the ALBA staff.

Appendix A. Supplementary data

Supplementary data to this article can be found online at https://doi.org/10.1016/j.cej.2025.171198.

Data availability

Data will be made available on request.

References

[1] X.X. Wang, M.T. Swihart, G. Wu, Achievements, challenges and perspectives on cathode catalysts in proton exchange membrane fuel cells for transportation, Nat. Catal. 2 (2019) 578–589, https://doi.org/10.1038/s41929-019-0304-9.
[2] J. Zhang, Z. Xia, L. Dai, Carbon-based Electrocatalysts for advanced energy conversion and storage, Sci. Adv. 1 (2015) e1500564, https://doi.org/10.1126/sciadv.1500564.
[3] Y. Sun, M. Delucchi, J. Ogden, The impact of widespread deployment of fuel cell vehicles on platinum demand and Price, Int. J. Hydrog. Energy 36 (2011) 11116–11127, https://doi.org/10.1016/j.ijhydene.2011.05.157.
[4] R. Martinez-Hincapie, V. Čolić, Electrocatalysts for the oxygen reduction reaction: from bimetallic platinum alloys to complex solid solutions, Chem. Eng. 6 (2022) 19, https://doi.org/10.3390/chemengineering6010019.
[5] Y. Nie, L. Li, Z. Wei, Recent advancements in Pt and Pt-free catalysts for oxygen reduction reaction, Chem. Soc. Rev. 44 (2015) 2168–2201, https://doi.org/10.1039/C4CS00484A.
[6] A. Eguizabal, L. Uson, V. Sebastian, J.L. Hueso, M.P. Pina, Efficient and facile tuning of Vulcan XC72 with ultra-small Pt nanoparticles for Electrocatalytic applications, RSC Adv. 5 (2015) 90691–90697, https://doi.org/10.1039/C5RA16698E.
[7] M. Klingele, C. Van Pham, A. Fischer, S. Thiele, A review on metal-free doped carbon materials used as oxygen reduction catalysts in solid electrolyte proton exchange fuel cells, Fuel Cells 16 (2016) 522–539, https://doi.org/10.1002/fuce.201600113.
[8] L. Yang, J. Shui, L. Du, Y. Shao, J. Liu, L. Dai, Z. Hu, Carbon-based metal-free ORR Electrocatalysts for fuel cells: past, present, and future, Adv. Mater. 31 (2019) 1804799, https://doi.org/10.1002/adma.201804799.
[9] H. Osgood, S.V. Devaguptapu, H. Xu, J. Cho, G. Wu, Transition Metal (Fe, Co, Ni, and Mn) Oxides for Oxygen Reduction and Evolution Bifunctional Catalysts in Alkaline Media, Nano Today 11 (2016) 601–6025, https://doi.org/10.1016/j.nantod.2016.09.001.
[10] W. Gu, L. Hu, J. Li, E. Wang, Recent advancements in transition metal-nitrogen-carbon catalysts for oxygen reduction reaction, Electroanalysis 30 (2018) 1217–1228, https://doi.org/10.1002/elan.201700780.
[11] S. Maldonado, K.J. Stevenson, Influence of nitrogen doping on oxygen reduction Electrocatalysis at carbon nanofiber electrodes, J. Phys. Chem. B 109 (2005) 4707–4716, https://doi.org/10.1021/jp044442z.
[12] S. Wang, D. Yu, L. Dai, Polyelectrolyte functionalized carbon nanotubes as efficient metal-free Electrocatalysts for oxygen reduction, J. Am. Chem. Soc. 133 (2011) 5182–5185, https://doi.org/10.1021/ja1112904.
[13] B. Li, L. Zhang, J. Zhang, Y. Su, Recent insight in transition metal anchored on nitrogen-doped carbon catalysts: preparation and catalysis application, Electrochem 3 (2022) 520–537, https://doi.org/10.3390/electrochem3030036.
[14] F. Dong, M. Wu, Z. Chen, G. Zhang, J. Qiao, S. Sun, Atomically dispersed transition metal-nitrogen-carbon bifunctional oxygen Electrocatalysts for zinc-air batteries: recent advances and future perspectives, Nano-Micro Lett. 14 (2022) 36, https://doi.org/10.1007/s40820-021-00768-3.
[15] P. Wei, X. Sun, Q. Liang, X. Li, Z. He, X. Hu, J. Zhang, M. Wang, Q. Li, H. Yang, J. Han, Y. Huang, Enhanced oxygen evolution reaction activity by encapsulating NiFe alloy nanoparticles in nitrogen-doped carbon nanofibers, Appl. Mater. Interfaces 12 (2020) 31503–31513, https://doi.org/10.1021/acsami.0c08271.
[16] Y. Chen, S. Ji, C. Chen, Q. Peng, D. Wang, Y. Li, Single-atom catalysts: synthetic strategies and electrochemical applications, Joule 2 (2018) 1242–1264, https://doi.org/10.1016/j.joule.2018.06.019.
[17] J. Kim, S. Choi, J. Cho, S.Y. Kim, H.W. Jang, Toward multicomponent single-atom catalysis for efficient electrochemical energy conversion, ACS Mater. Au 2 (2022) 1–20, https://doi.org/10.1021/acsmaterialsau.1c00041.
[18] Š. Kment, A. Bakandritsos, I. Tantis, H. Kmentová, Y. Zuo, O. Henrotte, A. Naldoni, M. Otyepka, R.S. Varma, R. Zbořil, Single atom catalysts based on earth-abundant metals for energy-related applications, Chem. Rev. 124 (2024) 11767–11847, https://doi.org/10.1021/acs.chemrev.4c00155.
[19] A. Wang, J. Li, T. Zhang, Heterogeneous Single-Atom Catalysis, Nat. Rev. Chem. 2 (2018) 65–81, https://doi.org/10.1038/s41570-018-0010-1.
[20] Z.W. Chen, L.X. Chen, C.C. Yang, Q. Jiang, Atomic (single, double, and triple atoms) catalysis: Frontiers, opportunities, and challenges, J. Mater. Chem. A 7 (2019) 3492–3515, https://doi.org/10.1039/C8TA11416A.
[21] X. Li, et al., Microenvironment modulation of single-atom catalysts and their roles in electrochemical energy conversion, Sci. Adv. 6 (2020) eabb6833, https://doi.org/10.1126/sciadv.abb6833.
[22] S. Das, J. Pérez-Ramírez, J. Gong, N. Dewangan, K. Hidajat, B.C. Gates, S. Kawi, Core–Shell Structured Catalysts for Thermocatalytic, Photocatalytic, and Electrocatalytic Conversion of CO_2, Chem. Soc. Rev. 49 (2020) 2937–3004, https://doi.org/10.1039/C9CS00713J.
[23] A. Madrid, Á. Tolosana-Moranchel, Á. García, S. Rojas, F. Bartolome, E. Pakrieva, L. Simonelli, G. Martinez, J.L. Hueso, J. Santamaria, Laser-driven generation of single atom Fe-N-C catalysts for the oxygen reduction reaction, Chem. Eng. J. 498 (2024) 155363, https://doi.org/10.1016/j.cej.2024.155363.
[24] X. Zhang, C. Gao, L. Li, X. Yan, N. Zhang, J. Bao, Fe-based MOF encapsulating Triethylenediamine cobalt complex to prepare a FeN_3–CoN_3 dual-atom catalyst for efficient ORR in Zn–air batteries, J. Colloid Interface Sci. 676 (2024) 871–883, https://doi.org/10.1016/j.jcis.2024.07.176.
[25] A. Han, W. Sun, X. Wan, D. Cai, X. Wang, F. Li, J. Shui, D. Wang, Construction of co_4 atomic clusters to enable Fe–N_4 motifs with highly active and durable oxygen reduction performance, Angew. Chem. Int. Ed. 62 (2023) e202303185, https://doi.org/10.1002/anie.202303185.
[26] R. Dun, X. He, J. Huang, W. Wang, Y. Liu, L. Li, B. Lu, Z. Hua, J. Shi, Atomically dispersed Fe/co dual site Electrocatalysts derived from covalent Triazine frameworks for boosting oxygen reduction, J. Mater. Chem. A 11 (2023) 5902–5909, https://doi.org/10.1039/D3TA00307H.
[27] M. Ferrandon, A.J. Kropf, D.J. Myers, K. Artyushkova, U. Kramm, P. Bogdanoff, G. Wu, C.M. Johnston, P. Zelenay, Multitechnique characterization of a polyaniline–Iron–carbon oxygen reduction catalyst, J. Phys. Chem. C 116 (2012) 16001–16013, https://doi.org/10.1021/jp302396g.
[28] L.T. Soo, K.S. Loh, A.B. Mohamad, W.R. Wan Daud, W.Y. Wong, Effect of nitrogen precursors on the electrochemical performance of nitrogen-doped reduced graphene oxide towards oxygen reduction reaction, J. Alloys Compd. 677 (2016) 112–120, https://doi.org/10.1016/j.jallcom.2016.03.214.
[29] Y. Zeng, C. Li, B. Li, X. Wang, Y. Zhang, Z. Liu, Y. Chen, S. Wang, X. Zhou, B. Han, J. Zhang, Y. Li, H. Liu, H. Wang, Y. Liu, Tuning the Thermal Activation Atmosphere Breaks the Activity–Stability Trade-Off of Fe–N–C Oxygen Reduction Fuel Cell Catalysts, Nat. Catal. 6 (2023) 1215–1227, https://doi.org/10.1038/s41929-023-01062-8.
[30] J. Wang, H. Kong, J. Zhang, Y. Hao, Z. Shao, F. Ciucci, Carbon-based electrocatalysts for sustainable energy applications, Prog. Mater. Sci. 116 (2021) 100717, https://doi.org/10.1016/j.pmatsci.2020.100717.
[31] A. Madrid, A. Martín-Pardillos, J. Bonet-Aleta, M. Sancho-Albero, G. Martinez, J. Calzada-Funes, P. Martin-Duque, J. Santamaria, J.L. Hueso, Nitrogen-doped carbon Nanodots deposited on Titania nanoparticles: unconventional near-infrared active Photocatalysts for Cancer therapy, Catal. Today 419 (2023) 114154, https://doi.org/10.1016/j.cattod.2023.114154.
[32] A. Madrid, G. Martinez, F. Hornos, J. Bonet-Aleta, E. Calvo, A. Lozano, J.L. Hueso, Laser-induced tuning of carbon Nanosensitizers to maximize nitrogen doping and reactive oxygen species production in the visible range, Catal. Today 422 (2023) 114214, https://doi.org/10.1016/j.cattod.2023.114214.
[33] N. Mas, J.L. Hueso, G. Martínez, A. Madrid, R. Mallada, M.C. Ortega-Liebana, J. Santamaría, Laser-driven direct synthesis of carbon Nanodots and application as sensitizers for visible-light Photocatalysis, Carbon 156 (2020) 453–462, https://doi.org/10.1016/j.carbon.2019.09.073.
[34] M. Hara, T. Yoshida, A. Takagaki, T. Takata, J.N. Kondo, S. Hayashi, K. Domen, A carbon material as a strong protonic acid, Angew. Chem. Int. Ed. 43 (2004) 2955–2958, https://doi.org/10.1002/anie.200453947.
[35] A. Cuesta, P. Dhamelincourt, J. Laureyns, A. Martínez-Alonso, J.M.D. Tascón, Raman microprobe studies on carbon materials, Carbon 32 (1994) 1523–1532, https://doi.org/10.1016/0008-6223(94)90148-1.
[36] M. Thommes, Physical adsorption characterization of Nanoporous materials, Chem. Ing. Tech. 82 (2010) 1059–1073, https://doi.org/10.1002/cite.201000064.
[37] Y. Jiang, L. Yang, T. Sun, J. Zhao, Z. Lyu, O. Zhuo, X. Wang, Q. Wu, J. Ma, Z. Hu, Significant contribution of intrinsic carbon defects to oxygen reduction activity, ACS Catal. 5 (2015) 6707–6712, https://doi.org/10.1021/acscatal.5b01835.
[38] F. Jaouen, F. Charreteur, J.P. Dodelet, Fe-based catalysts for oxygen reduction in PEMFCs: importance of the disordered phase of the carbon support, J. Electrochem. Soc. 153 (2006) A689–A698, https://doi.org/10.1149/1.2168418.
[39] K.B. Bota, G.M.K. Abotsi, Ammonia: a reactive medium for catalysed coal gasification, Fuel 73 (1994) 1354–1357, https://doi.org/10.1016/0016-2361(94)90313-1.
[40] R. Zhao, Z. Liang, S. Gao, C. Yang, B. Zhu, J. Zhao, C. Qu, R. Zou, Q. Xu, Puffing Up Energetic Metal–Organic Frameworks to Large Carbon Networks with Hierarchical Porosity and Atomically Dispersed Metal Sites, Angew. Chem. Int. Ed. 58 (2019) 1975–1979, https://doi.org/10.1002/anie.201811126.
[41] D. Liu, K. Ni, J. Ye, J. Xie, Y. Zhu, S,N Co-Doped Carbon Nanotube Encased Co NPs as Efficient Bifunctional Oxygen Electrocatalysts for Zinc-Air Batteries, Chem. Eng. J. 422 (2021) 130134, https://doi.org/10.1016/j.cej.2021.130135.
[42] D. Liu, K. Ni, J. Ye, J. Xie, Y. Zhu, L. Song, Tailoring the structure of carbon nanomaterials toward high-end energy applications, Adv. Mater. 30 (2018) 1802104, https://doi.org/10.1002/adma.201802104.
[43] A.B. Jorge, R. Jervis, A.P. Periasamy, M. Qiao, J. Feng, L.N. Tran, M.-M. Titirici, 3D carbon materials for efficient oxygen and hydrogen Electrocatalysis, Adv. Energy Mater. 10 (2020) 1902494, https://doi.org/10.1002/aenm.201902494.

[44] D. Long, W. Li, L. Ling, J. Miyawaki, I. Mochida, S.-H. Yoon, Preparation of nitrogen-doped graphene sheets by a combined chemical and hydrothermal reduction of graphene oxide, Langmuir 26 (2010) 16096–16102, https://doi.org/10.1021/la102425a.
[45] J.L. Hueso, J.P. Espinós, A. Caballero, J. Cotrino, A.R. González-Elipe, XPS investigation of the reaction of carbon with NO, O_2, N_2, and H_2O plasmas, Carbon 45 (2007) 89–96, https://doi.org/10.1016/j.carbon.2006.07.021.
[46] J.R. Pels, F. Kapteijn, J.A. Moulijn, Q. Zhu, K.M. Thomas, Evolution of nitrogen functionalities in carbonaceous materials during pyrolysis, Carbon 33 (1995) 1641–1653, https://doi.org/10.1016/0008-6223(95)00154-6.
[47] O.L. Li, Y. Wada, A. Kaneko, H. Lee, T. Ishizaki, Oxygen reduction reaction activity of thermally tailored nitrogen-doped carbon electrocatalysts prepared through plasma synthesis, ChemElectroChem 5 (2018) 1995–2001, https://doi.org/10.1002/celc.201800063.
[48] D. Bar-Tow, E. Peled, L. Burstein, A study of highly oriented pyrolytic graphite as a model for the graphite anode in Li-ion batteries, J. Electrochem. Soc. 146 (1999) 824, https://doi.org/10.1149/1.1391688.
[49] D.-S. Yang, M.Y. Song, K.P. Singh, J.-S. Yu, The role of iron in the preparation and oxygen reduction reaction activity of nitrogen-doped carbon, Chem. Commun. 51 (2015) 2450–2453, https://doi.org/10.1039/C4CC08592B.
[50] V. Monini, M. Bonechi, C. Bazzicalupi, A. Bianchi, P. Gentilesca, W. Giurlani, M. Innocenti, A. Meoli, G.M. Romano, M. Savastano, Oxygen reduction reaction (ORR) in alkaline solution catalysed by an atomically precise catalyst based on a Pd (II) complex supported on multi-walled carbon nanotubes (MWCNTs). Electrochemical and structural considerations, Dalton Trans. 53 (2024) 2487–2500, https://doi.org/10.1039/D3DT03947A.
[51] A.A. Kulikovsky, The voltage–current curve of a polymer electrolyte fuel cell: "exact" and fitting equations, Electrochem. Commun. 4 (2002) 845, https://doi.org/10.1016/S1388-2481(02)00466-6.
[52] J. Wang, C.-X. Zhang, J. Liu, D. Ren, B. Li, J. Huang, Q. Zhang, Quantitative kinetic analysis on oxygen reduction reaction: a perspective, Nano Mater. Sci. 3 (2021) 313–318, https://doi.org/10.1016/j.nanoms.2021.03.006.
[53] J. Hernández-Ferrer, M. Gracia-Martín, A.B. Benito, W.K. Maser, E. García-Bordejé, Effect of temperature and presence of minor amount of metal on porous carbon materials derived from ZIF8 pyrolysis for electrocatalysis, Catal. Today 423 (2023) 113993, https://doi.org/10.1016/j.cattod.2022.12.024.
[54] Q. Lv, W. Si, J. He, L. Sun, C. Zhang, N. Wang, Z. Yang, X. Li, X. Wang, W. Deng, Y. Long, C. Huang, Y. Li, Selectively nitrogen-doped carbon materials as superior metal-free catalysts for oxygen reduction, Nat. Commun. 9 (2018) 3376, https://doi.org/10.1038/s41467-018-05878-y.
[55] A.R. Mainar, O. Leonet, M. Bengoechea, I. Boyano, I. Meatza, A. Kvasha, A. Guerfi, J.A. Blázquez, Alkaline aqueous electrolytes for secondary zinc–air batteries: an overview, Int. J. Energy Res. 40 (2016) 1032–1049, https://doi.org/10.1002/er.3499.
[56] C. Domínguez, F.J. Pérez-Alonso, J.L. Gómez de la Fuente, S.A. Al-Thabaiti, S. N. Basahel, A.O. Alyoubi, A.A. Alshehri, M.A. Peña, S. Rojas, Influence of the electrolyte for the oxygen reduction reaction with Fe/N/C and Fe/N/CNT electrocatalysts, J. Power Sources 271 (2014) 87–96, https://doi.org/10.1016/j.jpowsour.2014.07.173.
[57] Á. García, L. Pascual, P. Ferrer, D. Gianolio, G. Held, D.C. Grinter, M.A. Peña, M. Retuerto, S. Rojas, Study of the evolution of FeNxCy and Fe3C species in Fe/N/C catalysts during the oxygen reduction reaction in acid and alkaline electrolyte, J. Power Sources 490 (2021) 229487, https://doi.org/10.1016/j.jpowsour.2021.229487.
[58] H. Mistry, A.S. Varela, S. Kuhl, P. Strasser, B.R. Cuenya, Nanostructured electrocatalysts with tunable activity and selectivity, Nat. Rev. Mater. 1 (2016) 16009, https://doi.org/10.1038/natrevmats.2016.9.
[59] Y. Shao, J.-P. Dodelet, G. Wu, P. Zelenay, PGM-free cathode catalysts for PEM fuel cells: a mini-review on stability challenges, Adv. Mater. 31 (2019) 1807615, https://doi.org/10.1002/adma.201807615.
[60] J.K. Nørskov, J. Rossmeisl, A. Logadottir, L. Lindqvist, J.R. Kitchin, T. Bligaard, H. Jónsson, Origin of the Overpotential for oxygen reduction at a fuel-cell cathode, J. Phys. Chem. B 108 (2004) 17886–17892, https://doi.org/10.1021/jp047349j.
[61] B. Tang, Q. Ji, X. Zhang, R. Shi, J. Ma, Z. Zhuang, M. Sun, et al., Symmetry breaking of FeN_4 moiety via edge defects for acidic oxygen reduction reaction, Angew. Chem. 137 (2025) 13, https://doi.org/10.1002/anie.202424135.
[62] W. Yang, X. Liu, X. Yue, J. Jia, S. Guo, Bamboo-like carbon nanotube/Fe3C nanoparticle hybrids and their highly efficient catalysis for oxygen reduction, J. Am. Chem. Soc. 137 (2015) 1436–1443, https://doi.org/10.1021/ja5129132.
[63] J. Liang, Y. Jiao, M. Jaroniec, S.Z. Qiao, Sulfur and nitrogen dual-doped mesoporous graphene electrocatalyst for oxygen reduction with synergistically enhanced performance, Angew. Chem. Int. Ed. 51 (2012) 11496, https://doi.org/10.1002/anie.201206720.
[64] Z. Luo, S. Lim, Z. Tian, J. Shang, L. Lai, B. MacDonald, C. Fu, Z. Shen, T. Yu, J. Lin, Pyridinic N doped graphene: synthesis, electronic structure, and electrocatalytic property, J. Mater. Chem. 21 (2011) 8038, https://doi.org/10.1039/C1JM10845J.
[65] L. Zhang, W. Sang, T. Wang, X. Wei, Z. Li, C. Chen, Z. Kou, et al., Cu–N–C support confinement stabilizes active co sites in oxygen reduction reaction, Nano Res. 18 (2025), https://doi.org/10.26599/NR.2025.94907345, 9490–7345.
[66] M.S. Thorum, J.M. Hankett, A.A. Gewirth, Poisoning the oxygen reduction reaction on carbon-supported Fe and cu electrocatalysts: evidence for metal-centered activity, Phys. Chem. Chem. Phys. 2 (2011) 295–298, https://doi.org/10.1021/jz1016284.
[67] F. Kong, X. Cui, Y. Huang, H. Yao, Y. Chen, H. Tian, G. Meng, C. Chen, Z. Chang, J. Shi, N-doped carbon Electrocatalyst: marked ORR activity in acidic media without the contribution from metal sites? Angew. Chem. Int. Ed. 61 (2022) e202116290 https://doi.org/10.1002/ange.202116290.
[68] X. Jin, Y. Jiang, Q. Hu, S. Zhang, Q. Jiang, L. Chen, L. Xu, Y. Xie, J. Huang, Highly efficient electrocatalysts with $CoO/CoFe_2O_4$ composites embedded within N-doped porous carbon materials prepared by hard-template method for oxygen reduction reaction, RSC Adv. 7 (2017) 56375–56381, https://doi.org/10.1039/C7RA09517A.
[69] P. Wei, X. Li, Z. He, X. Sun, Q. Liang, Z. Wang, C. Fang, Q. Li, H. Yang, J. Han, Y. Huang, Porous N, B co-doped carbon nanotubes as efficient metal-free electrocatalysts for ORR and Zn-air batteries, Chem. Eng. J. 422 (2021) 130134, https://doi.org/10.1016/j.cej.2021.130134.
[70] J. Zhang, Z. Zhao, Z. Xia, A metal-free bifunctional electrocatalyst for oxygen reduction and oxygen evolution reactions, Nat. Nanotechnol. 10 (2015) 444–452, https://doi.org/10.1038/nnano.2015.48.
[71] P. Cai, S. Ci, E. Zhang, P. Shao, C. Cao, Z. Wen, FeCo alloy nanoparticles confined in carbon layers as high-activity and robust cathode catalyst for Zn-air battery, Electrochim. Acta 220 (2016) 354–362, https://doi.org/10.1016/j.electacta.2016.10.070.
[72] M. Liu, F. Yu, C. Ma, X. Xue, H. Fu, H. Yuan, S. Yang, G. Wang, X. Guo, L. Zhang, Effective oxygen reduction reaction performance of FeCo alloys in situ anchored on nitrogen-doped carbon by the microwave-assisted carbon bath method and subsequent plasma etching, Nanomaterials 9 (2019) 1284, https://doi.org/10.3390/nano9091284.
[73] L. Lin, Q. Zhu, A.-W. Xu, Noble-metal-free Fe–N/C catalyst for highly efficient oxygen reduction reaction under both alkaline and acidic conditions, J. Am. Chem. Soc. 136 (2014) 11027–11033, https://doi.org/10.1021/ja504696r.
[74] M.M. Hossen, K. Artyushkova, P. Atanassov, A. Serov, Synthesis and characterization of high performing Fe-N-C catalyst for oxygen reduction reaction (ORR) in alkaline exchange membrane fuel cells, J. Power Sources 375 (2018) 214–221, https://doi.org/10.1016/j.jpowsour.2017.07.084.
[75] Q.-L. Zhu, W. Xia, T. Akita, R. Zou, Q. Xu, Metal-organic framework-derived honeycomb-like open porous nanostructures as precious-metal-free catalysts for highly efficient oxygen electroreduction, Adv. Mater. 28 (2016) 6391–6398, https://doi.org/10.1002/adma.201600979.
[76] J. Hernández-Ferrer, M. Gracia-Martín, A.M. Benito, W.K. Maser, E. García-Bordejé, Effect of temperature and presence of minor amount of metal on porous carbon materials derived from ZIF-8 pyrolysis for electrocatalysis, Catal. Today 423 (2023) 113618, https://doi.org/10.1016/j.cattod.2022.12.024.
[77] Y. Qi, K. Song, Q. Liang, X. Zhou, M. Liu, W. Li, F. Liu, et al., Asymmetric B-coordination stimulated high-spin cobalt boosts ORR, Nano Res. 18 (2025), https://doi.org/10.26599/NR.2025.94907278, 9490–7278.